Interatomic potential to study plastic deformation in tungsten-rhenium alloys

G Bonny, A. Bakaev, D. Terentyev, Yu.A. Mastrikov

Interatomic potential to study plastic deformation in tungsten-rhenium alloys

G. Bonny[1,*], A. Bakaev[1], D. Terentyev[1] and Yu.A. Mastrikov[2]

[1] SCK•CEN, Nuclear Materials Science Institute, Boeretang 200, B-2400 Mol, Belgium.

[2] University of Latvia, Institute for Solid State Physics, Kengaraga str. 8, Riga, Latvia.

Abstract

In this work an interatomic potential for the W-Re system is fitted and benchmarked against experimental and density functional theory (DFT) data, of which part are generated in this work. Having in mind studies related to the plasticity of W-Re alloys under irradiation, emphasis is put on fitting point-defect properties, elastic constants and dislocation properties. The developed potential can reproduce the mechanisms responsible for the experimentally observed softening, i.e., decreasing shear moduli, decreasing Peierls barrier and asymmetric screw dislocation core structure with increasing Re content in W-Re solid solutions. In addition the potential predicts elastic constants in reasonable agreement with DFT data for the phases forming non-coherent precipitates (σ- and χ-phases) in W-Re alloys. In addition, the mechanical stability of the different experimentally observed phases is verified in the temperature range of interest (700-1500 K). As a conclusion the presented potential provides an excellent tool to study plasticity in W-Re alloys at the atomic level.

1. Introduction

The international programme on thermonuclear fusion power requires the selection and qualification of materials for extreme environmental conditions, including high heat, charge particle flux and high energy neutron loads [1]. High strength refractory metals, with tungsten (W) in particular, are materials that will play an important role in both the ITER and DEMO projects [2-4]. For ITER, W is selected as a divertor material while for DEMO it will also serve as first wall armor material. Because of its high melting temperature and resistance to

---

sputtering by low-energy ions, W is a promising plasma facing material for both the divertor and first wall.

However, the main drawback of W for structural and armor applications is its high ductile-to-brittle transition temperature (DBTT), being around 300-400 °C [5]. In addition to this, neutron irradiation is known to further embrittle the material, see for example [6-8]. As mentioned in the Fusion Material Assessment Group report, the intrinsic brittleness of W is one of the major risks imposed on the design of plasma-facing and high heat flux components, especially given the lack of data on its evolution with neutron dose [9]. Therefore, the investigation of ductile properties of W and the underlying mechanisms of plastic deformation are important for the development of advanced W-based alloys as well as for understanding baseline tungsten, i.e., commercially pure polycrystalline tungsten.

Although the use of industrially pure W is considered, the production of rhenium (Re) under neutron irradiation will occur as a result of transmutation reactions induced by thermal neutrons and the concentration established under expected DEMO conditions will reach several percents at a dose of 10 dpa [10]. This irradiation-induced chemical modification is proven to have a strong impact on the microstructural evolution of the material in terms of accumulation of dislocation loops, voids and Re-rich precipitates [6, 11].

In absence of irradiation, solid solution alloying of W by Re has been shown to reduce its shear modulus (<10% Re) [12], the hardness (<10% Re) [13], and the brittleness (<25% Re) [14]. However, starting from ~10% Re the hardness and yield point increase due to solid solution hardening and above ~25% Re the alloy embrittles (and hardens) due to the formation of σ-phase precipitates (see [13] and references therein). Under irradiation, as the dose increases the microstructure is primary populated by dislocation loops (up to 0.1 dpa), then voids emerge (0.1-1 dpa) and then non-coherent precipitates start to form [6, 11]. Thus, Re solid solution has an important impact on the mechanical properties of W in both irradiation and non-irradiation conditions. Therefore, a deep understanding of the physical mechanisms by which Re comes into play is an important line of research.

In recent years the investigation of plastic deformation and the radiation-induced micro-structure makes intensive use of computer models that serve to complement and rationalize experimental studies. Modern computational materials science dealing with plasticity phenomena underlines the role played by dislocations and grain boundaries, which define the plastic deformation mechanisms at atomic and meso-scale (see for example [15-17]). The desired mechanical properties of a material tested under given conditions can be rationalized on the basis of crystal plasticity theory and its numerical implementation via

constitutive laws, including both irradiation and non-irradiation conditions (see for example [18, 19]). At present, many efforts are ongoing to explore the relationship between microstructure and mechanical response by advanced computational models (see for example [17, 20, 21]).

The main input parameters required for micro-mechanical models include precise information about the mobility of dislocations, the thermal activation of their glide, the impact of solid solution on the latter and interaction rules with radiation induced defects. Atomistic simulations represent the most natural tool to explore the above listed processes and feed meso-scale models with relevant data. Radiation induced defects, as experimentally observed in W under fusion relevant neutron irradiation conditions, have a size ranging from one to several nano-meters with a density of 10^{22}-10^{23} m^{-3}. This implies that an adequate simulation volume must contain from several hundred thousand to a few million atoms. The required simulation volume does not allow a quantum mechanical treatment of the system and therefore classical molecular dynamics (MD) using interatomic potentials must be used.

For metallic systems the embedded atom method (EAM) [22] is an excellent compromise between physical accuracy and computational efficiency. In the literature many EAM potentials exist for W (see [23] for an overview), but up to our knowledge none exists for Re and the W-Re system. Therefore, an EAM type potential for the W-Re system is developed in this work. Having in mind studies related to plasticity of W-Re alloys under irradiation, emphasis was put on fitting point-defect properties, elastic constants and dislocation properties.

For the purpose of fitting and benchmarking the EAM potential, we performed density functional theory (DFT) calculations. For this we focused on the interaction between Re atoms and point defects, the effect of Re on the ½<111> screw dislocation core structure, the <111> interrow potential, ½<111>{110} stacking fault energy profile and symmetric tilt grain boundaries. In addition the EAM potential was applied to calculate the elastic constants of the different experimental phases (bcc, σ, χ and hcp) and were compared to experiment and DFT data where available. It was checked that the latter phases are mechanically stable in the 700-1500 K temperature range. This temperature range is taken as guideline for the typical operation temperature of W as material for a plasma facing component surface in the water cooled divertor concept in the DEMO design [9].

2. Methods

2.1. Fitting strategy

In the literature, many EAM type interatomic potentials for bcc W are available (see [23] and references therein). A critical review assessing their strengths and weaknesses is given in [23]. In this work, we selected "EAM2" from the work by Marinica et al. [24], which gives good "overall performance". As key features, this potential provides elastic constants, point-defect, edge and screw dislocation properties as well as grain boundary energies consistent with DFT calculations or experiments (see [23] for more details). In addition, the potential was already applied as a part of W-H-He potentials [25] in the framework of the study of H and He retention in bcc W [26-28]. This choice guarantees a possible extension to the W-Re-H-He system.

Up to our knowledge, no EAM potential is available for hcp Re or the W-Re system and therefore they are fitted here. Prior to the cross interaction, an EAM potential for pure Re was fitted. The target material properties fitted here are the lattice stabilities of different crystallographic structures (bcc, fcc and hcp), their cohesive energy E_{coh}, and equilibrium lattice parameters, the five independent elastic constants for the equilibrium hcp lattice (C_{11}, C_{33}, C_{12}, C_{13}, C_{44}), the single vacancy formation energy and Rose's equation of state for the hcp lattice [29].

For the W-Re cross interaction, we considered the formation energy of a single Re atom, the binding energy between first (1nn) and second nearest neighbor (2nn) Re-v pairs, the Re-v migration barrier and binding energy of the <111> mixed W-Re dumbbell in bcc W. To insure a physical shape of the mixed pair potential, the latter was also fitted to Rose's equation of state for the σ-phase. As reference compound for the σ-phase we chose the compound with lowest formation energy reported in [30].

The fitting of an interatomic potential can be viewed as the problem of finding the potential parameters that allow the latter to optimally reproduce a given data set. Mathematically, it can be formulated as the minimization of the overall squared deviation, the so-called objective function, between predicted and reference data. For the details about different optimization strategies the reader is referred to [31, 32]. The parameterization and optimized parameters of the EAM potential are provided in Appendix A.

2.2. Benchmark calculations

The developed EAM potential is tested and validated against experimental and DFT data from the literature as well as to additional DFT data calculated in this work. In this section we summarize the settings for the DFT and EAM calculations.

The DFT calculations were performed using the Vienna ab initio simulation package (VASP 5.4) [33, 34]. VASP includes a plane-wave DFT code that implements the projector augmented wave (PAW) method [35, 36]. For consistency with our previous calculations (see [23]), standard PAW potentials supplied with VASP were used. The electron exchange-correlation functional was described within the generalized gradient approximation (GGA) using the Perdew–Wang [37] parameterization, with a Vosko-Wilk-Nusair interpolation [38].

For W and Re a potential was applied with six and seven valence electrons, respectively. The plane wave cut-off energy was set to 450 eV. Brillouin zone sampling was performed using the Monkhorst–Pack scheme [39], where the k-point meshes differ depending on the box size and both are given in Table 1. Finite-temperature smearing was obtained following the Methfessel–Paxton method [40] with a smearing width of 0.3 eV. Ionic relaxation was performed using the conjugate gradient optimization scheme with a force convergence criterion of 0.03 eVÅ^{-1} for each atom.

The EAM calculations were performed using the large-scale atomic molecular massively parallel simulator (LAMMPS) [41]. Ionic relaxation was performed using the conjugate gradient optimization scheme with a convergence criterion on the 2-norm of the global force vector of 10^{-10} eVÅ^{-1}. The specifics of box size and boundary conditions depend on the calculated property and are summarized in Table 1.

The elastic constants at finite temperature were obtained from MD simulations. The same configurations used for the zero K computations were first thermalized for 100 ps in NPT ensemble to obtain the equilibrium lattice constant. Then elastic constants were obtained from MD simulations in NVE ensemble averaged over 1 ps under different deformations. An averaging time of 30 ps and time step of 1 fs proved enough to obtain convergence in the resulting elastic constants.

The melting temperature, T_m, was obtained by applying an interface method. With this method T_m is defined as the temperature at which both solid and liquid phases coexist. Such simulations were performed using MD in NVE ensemble over 1 ns with a time step of 1 fs.

The point defect properties in bcc W were calculated using a simulation box with principal axes oriented along the [100], [010] and [001] directions. For all other properties in bcc W the principal axes of the simulation box were oriented along the [110], [$\bar{1}$12] and

$[1\bar{1}1]$ directions, except for grain boundary (GB) calculations, which all have different orientations of the axes depending on the GB type (see below).

For all EAM calculations the configurations were the same as for the DFT calculations, but the DFT box was duplicated several times in the $[110]$ and $[\bar{1}12]$ directions or GB plane so that the distance in either direction is at least two times the potential cut-off. Along the $[1\bar{1}1]$ direction or orthogonal to the GB plane this condition is already satisfied for DFT configurations. The latter condition is necessary to satisfy the minimum image criterion to avoid self-interaction of the interatomic potential. This set-up allows a one-to-one comparison between DFT and the potential.

The formation energy, $E_f(N_X,N_Y)$, of a configuration containing N_X X and N_Y Y (vacancy) atoms with a total of N atoms is computed as,

$$E_f(N_X, N_Y) = NE(N_X, N_Y) + N_X E(X) + N_Y E(Y), \tag{1}$$

with E the energy per atom of the given supercell. The reference state for W, Re and v is bcc, hcp and vacuum ($E(\text{v})=0$), respectively. Given E_f, the total binding energy between X-Y pairs in bcc W is computed as,

$$E_b(X - Y) = E_f(X,Y) - E_f(X) - E_f(Y). \tag{2}$$

The investigated GBs were prepared considering a mirror symmetry for bi-crystals. The principal axes of the crystals x, y and z correspond to the tilt axis, GB axis and normal to the GB plane, respectively. In both DFT and EAM calculations 3D periodic super cells were used and the GB energy, γ_{GB}, was calculated as,

$$\gamma_{GB} = \frac{E_{GB} - NE(W)}{2S}, \tag{3}$$

with E_{GB} the total energy of the crystal containing the GB.

Each GB in pure W was relaxed allowing for both ionic relaxation and relaxation along the z-axis. Then that configuration was used to insert a Re atom at different distances from the GB plane. At that point only ionic relaxation at constant volume was allowed. The binding energy between a Re atom and the GB is estimated as the total energy difference between the GB configuration with Re atom in the bulk and Re atom near the GB. The bulk

position is located at approximately equal distances form the GB planes. For the EAM calculations the resulting difference is divided by the total number of Re atoms contained in the supercell, which is larger than one due to the minimum image criterion.

In analogy with the GB calculations, for pure W the ½<111>{110} stacking fault energy profile was obtained allowing for both ionic relaxation and relaxation along the [110] direction. Then that configuration was used to insert a Re atom in the shear plane. At that point only ionic relaxation at constant volume was allowed.

Table 1 – Details of the calculation set-up for the different DFT and EAM calculations.

| Configuration | Periodicity | DFT | | | EAM | |
		N	Size (a_0^3)	k-points	N	Size (a_0^3)
Point defects in bcc W	3D	128	4×4×4	3×3×3	2000	10.0×10.0×10.0
Elastic Constants	3D					
bcc-phase		NC	NC	NC	2000	10.0×10.0×10.0
hcp-phase		NC	NC	NC	1200	8.8×7.6×8.5
σ-phase		NC	NC	NC	7500	15.4×15.4×16.1
χ-phase		NC	NC	NC	1566	9.3×9.3×9.3
<111> inter row potential	3D	72	4.2×4.9×1.7	3×3×9	216	4.2×4.9×5.1
½<111> screw dislocation core	2D	NC	NC	NC	18144	49.5×49.0×5.2
½<111>{110} stacking fault energy profile	2D	120	18.9×2.4×1.7	1×7×9	720	18.9×4.8×5.1
Grain boundaries	3D					
Σ3⟨110⟩{111}		144	2.8×2.4×10.6	5×7×1	576	5.6×4.8×10.6
Σ3⟨110⟩{112}		96	2.8×1.7×9.9	5×9×1	576	5.6×5.1×9.9
Σ5⟨100⟩{013}		240	2.0×3.2×19.1	7×5×1	1440	4.0×9.6×19.1

T_m	3D	NC	NC	NC	14400	28.5×59.3×139.8

NC indicates that the DFT values were not computed in this work.

3. Results

3.1. Pure potentials

As mentioned in Section 2.1 we chose "EAM2" from [24] to describe pure W. As key features, this potential provides elastic constants, point-defect, edge and screw dislocation properties as well as grain boundary energies consistent with DFT calculations or experiments (see [23] for more details).

The key properties of the Re EAM potential are summarized in Table 2. Clearly, EAM is in excellent agreement with the experimental equilibrium lattice [42] and cohesive energy [43]. The relative lattice stabilities between hcp and bcc/fcc were taken from DFT calculations [44]. EAM reproduces the order between the different lattices, but underestimates the relative stability between the phases, especially between bcc and hcp. The latter should have no influence for our target applications in the temperature range 700-1500 K.

The experimental elastic constants [45] are well reproduced by EAM, i.e., all values lay within 10% of experimental values. For completeness also the Voigt average for the bulk- (B_V) and shear modulus (G_V) are provided. A comparison of the energy change of hcp Re under uniform compression or expansion to Rose's equation of state is provided in Fig. 5 of Section 3.5 (see further).

As a target for the vacancy formation energy, $E_f(v)$, a rough estimate based on the heuristic formula ($T_m/1000$) [43, 46] was used. The fully relaxed value predicted by the EAM agrees well with this estimate.

The melting temperature of Re is included in Table 2. EAM overestimates T_m by 40%, but this shortcoming should have no influence on simulations in the target temperature range 700-1500 K.

To conclude, the linear thermal expansion coefficients (α_a^{hcp} and α_c^{hcp}) of Re obtained by EAM are compared to the experimental ones [72] (see also Fig. B1 in Appendix B). While for α_c^{hcp} agreement is excellent, EAM underestimates α_a^{hcp} by almost a factor three. This shortcoming, however, should have no influence on the target applications, i.e., plastic deformation in W-Re alloys.

Table 2 – Summary of the key properties of the Re EAM potential.

Property	Target	EAM
a (hcp) (Å)	2.761[a]	2.761
c/a (hcp)	1.614[a]	1.614
E_c(hcp) (eV)	8.03[b]	8.03
a (fcc) (Å)	3.928[c]	3.900
ΔE_c(hcp-fcc) (eV)	0.06[c]	0.02
a (bcc) (Å)	3.125[c]	3.048
ΔE_c(hcp-bcc) (eV)	0.32[c]	0.13
B_V (GPa)	372[b]	382
G_V (GPa)	180[d]	170
C_{11} (GPa)	613[d]	611
C_{33} (GPa)	683[d]	682
C_{12} (GPa)	270[d]	299
C_{13} (GPa)	206[d]	234
C_{44} (GPa)	163[d]	159
E_f(v) (eV)	3.46[e]	3.49
T_m (K)	3459[f]	4836
α_a^{hcp}	7.0×10^{-6} [g]	2.5×10^{-6}
α_c^{hcp}	5.0×10^{-6} [g]	4.2×10^{-6}

[a] Experiment – Room temperature (T=296 K), Ref. [42].

[b] Ref. [43].

[c] DFT data – Ref. [44].

[d] Experiment – Room temperature (T=298 K), Ref. [45].

[e] Based on the correlation E_f(v)=T_m/1000 [46], with T_m taken from [43].

[f] Experiment – Ref. [43].

[g] Experiment – Ref. [72].

3.2. Point defects

The key point-defect properties of Re in bcc W are summarized in Table 3. Whilst fitting the different point-defect properties the correct reproduction of both Re-v binding energy and the

9

formation energy of Re in bcc W, E_f(Re), proved not manageable. While the Re-v binding energy determines the binding of a Re atom to "open volume", E_f(Re) determines the solubility of Re in bcc W.

Here we opted to reproduce E_f(Re) such that full solubility is obtained above 700 K, which is the lower limit of the envisaged applications. Experimentally, a large solubility is expected at that temperature, i.e., ~25% Re below 1273 K [47]). The Re solubility at 700 K predicted by EAM was estimated following the methodology in [48]. Due to this choice, EAM predicts a E_b(Re-v) that is ~70% lower than the DFT value.

Both the W-v and Re-v migration barriers in bcc W, E_m, are slightly overestimated by EAM compared to DFT. The Re-v migration barrier is 0.05 eV lower than the W-v migration barrier, a feature that is well reproduced by EAM.

With respect to interstitial Re, both DFT and EAM predict the <111> mixed W-Re dumbbell as energetically most favorable configuration, with the same binding energy. The relative difference between the mixed <111> and <110> dumbbell, on the other hand, is large overestimated by EAM. The latter value gives the saddle point for on-site rotation of the mixed <111> W-Re dumbbell. However, for the envisaged application of plasticity this shortcoming is of minor importance.

Table 3 – Summary of the key point-defect properties of the EAM potential. Properties indicated by * were included in the fit.

Property	DFT (eV)	EAM (eV)
E_f(Re) *	0.17[a]	0.17
E_b^{1nn}(Re-v) *	0.20[b] 0.22[c] 0.23[d]	0.06
E_b^{2nn}(Re-v) *	0.20[b] 0.22[c]	0.06
E_m(W-v)	1.69[c] 1.78[e]	1.85
E_m(Re-v) *	1.65[c]	1.81
$E_b^{\langle 111 \rangle}$(W-Re) *	0.79[c] 0.80[d]	0.80
$E_f^{\langle 111 \rangle}$(W-Re)	9.17[c] 9.53[a]	6.56
$\Delta E_f^{\langle 111 \rangle - \langle 110 \rangle}$(W-Re)	0.03[c] 0.02[a]	0.42
$\Delta E_f^{\langle 111 \rangle - \langle 100 \rangle}$(W-Re)	1.03[c]	1.68
$\Delta E_f^{\langle 111 \rangle - Tetra}$(Re)	1.36[c]	1.54
$\Delta E_f^{\langle 111 \rangle - Octa}$(Re)	2.15[c]	1.68

[a] DFT, [49].

[b] DFT, this work.

[c] DFT, [50].

[d] DFT, [51].

[e] DFT, [52].

3.3. Line defects

The ½<111> atomic row displacement energy curve, or interrow potential (IRP), calculated by both DFT and EAM is presented in Fig. 1. The IRP profile provides a measure of the energy barrier that must be overcome for the movement of a ½<111> screw dislocation. The DFT data show that the addition of a Re atom (one Re per $2b$) at 1nn distance to the displaced row marginally lowers the energy profile. In the case of EAM, the addition of Re has a negligible effect, thus consistent with the DFT data. This observation is consistent with the decrease in Peierls barrier for a ½<111> screw dislocation due to the alloying with Re, as discussed in [53]. The wide plateau near the center of the reaction path is not reproduced by EAM. This property is inherent to the used EAM potential for pure W, as discussed in [23]. We note that the IRP profile was not included in the fit of the EAM potential.
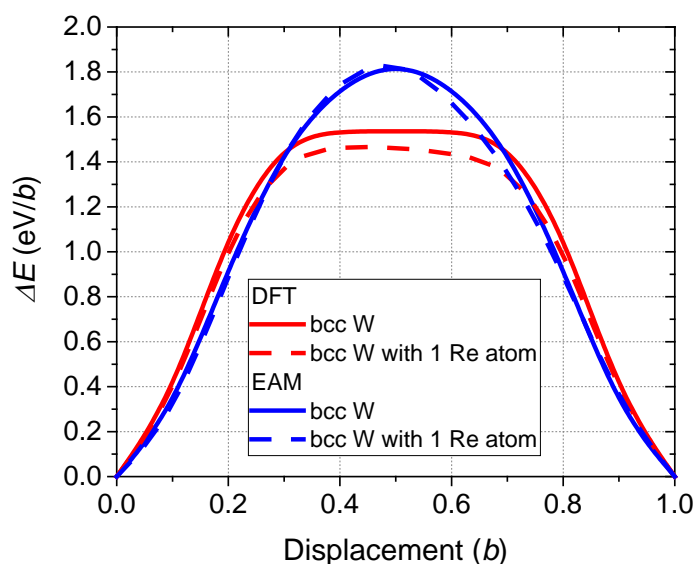

Fig. 1 – Comparison of the ½<111> IRP profile calculated by DFT and EAM with and without a Re atom at 1nn distance of the moving row.

In Fig. 2 the screw dislocation (SD) core structure is visualized by means of differential displacement maps [54] using EAM. It is well established by different DFT calculations that a SD in bcc transition metals and W in particular, exhibits a compact isotropic core structure [53, 55-61], a feature that is well the W EAM potential (see Fig. 2a and [23]). Consistent with the DFT calculations by Romaner et al [53], EAM predicts that the alloying of W by Re changes the SD core from a compact symmetric to a degenerate asymmetric structure (see Figs 2b, c and d). The introduction of a single Re atom into the SD core already leads to the breaking of its symmetry (see Fig. 2b). Further alloying of W with Re (for reasons of comparison with [53] we chose 25% Re) leads to a fully degenerate asymmetric SD core, regardless of the Re distribution. The latter is illustrated by two different local random arrangements of Re atoms around the SD core, with the Re arrangement in Fig. 2c denser than the one in Fig. 2d.
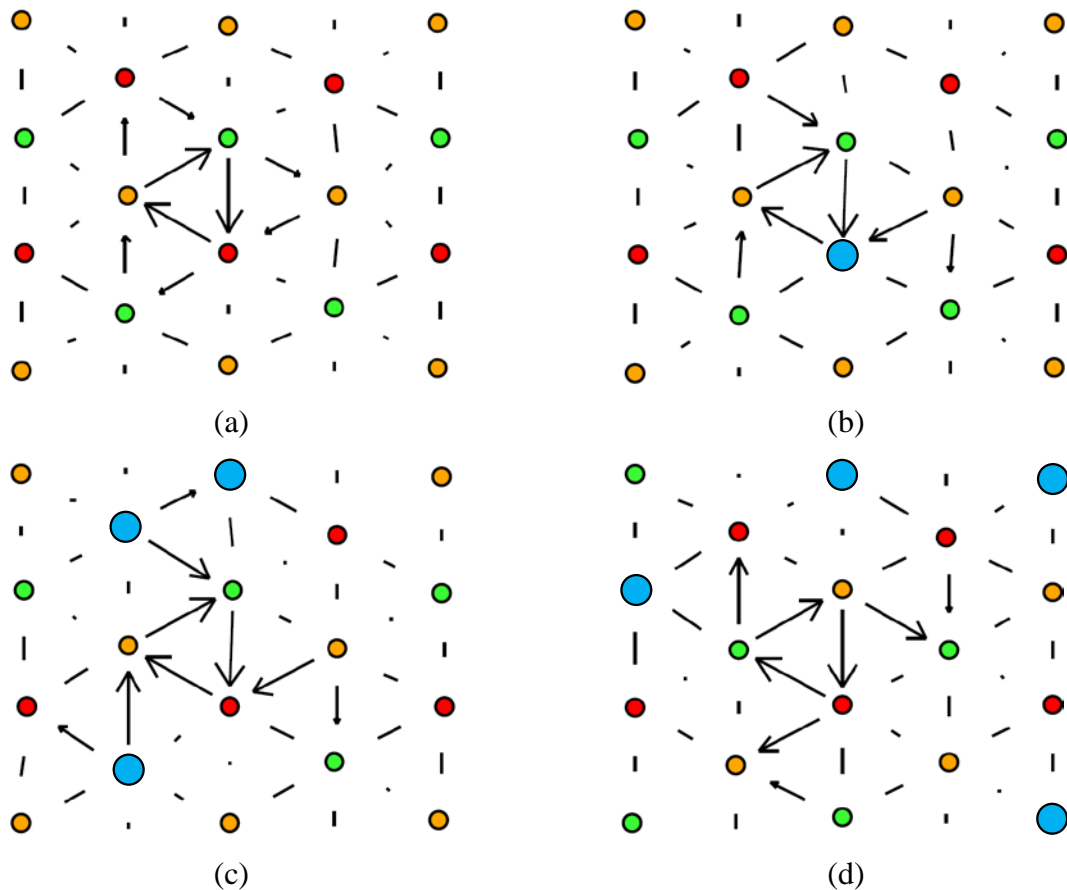

(a) (b)

(c) (d)

Fig. 2 – Differential displacement maps illustrating the screw dislocation core structure calculated by EAM in (a) pure W; (b) pure W with one Re atom in the core; representative snapshot for a W-25%Re random alloy (c) with many Re atoms near the core and (d) fewer Re atoms near the core. The large circles indicate the Re atoms while the small ones indicate

W atoms. The different colored W atoms illustrate the three different non-equivalent {111} planes.

As discussed in [53], the alloying of W with Re leads to a degenerate asymmetric SD core, which in turn allows for the activation the {112} slip system. This, in combination with a negligible or slight reduction of the IRP or Peierls barrier, leads to the experimentally observed softening of W-Re solid solutions [12, 13]. All mechanisms leading to this phenomenon are well reproduced by EAM.

3.4. Surface Defects

The ½<111>{110} stacking fault energy (SFE) profiles calculated by both DFT and EAM are given in Fig. 3. The SFE profile represents a measure for the energy barrier that must be overcome for the movement of a ½<111>{110} edge dislocation. The DFT data show that the addition of a Re atom (one Re per $3\sqrt{2}a_0^2$) to the sheared {110} plane marginally decreases the maximum of the SFE profile. In the case of EAM, the addition of Re has a negligible effect, thus consistent with the DFT data. We note that this property was not included in the fit of the EAM potential.
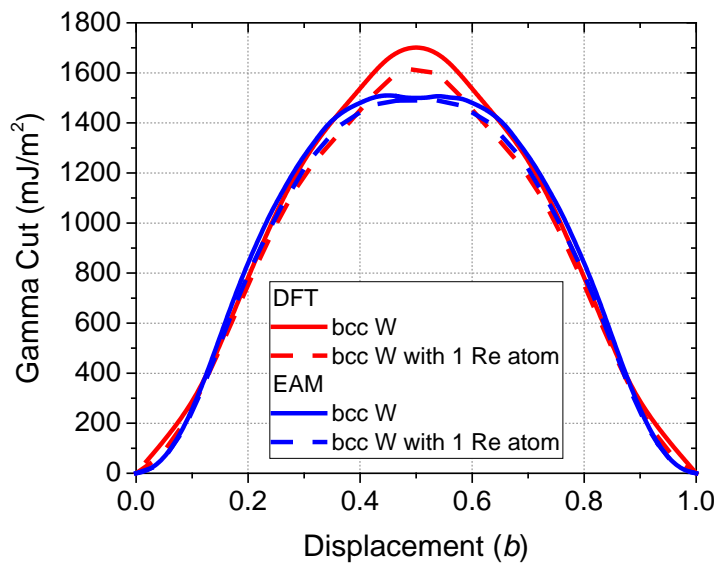

Fig. 3 – Comparison of the ½<111>{110} SFE profile calculated by DFT and EAM with and without a Re atom in the {110} shear plane.

A comparison between DFT and EAM for the GB energy, γ_{GB}, of different GBs is given in Table 4. Consistent with the calculations reported in [23, 62], DFT predicts the $\Sigma3\langle110\rangle\{112\}$ GB to have the lowest γ_{GB}, followed by both $\Sigma3\langle110\rangle\{111\}$ and $\Sigma5\langle100\rangle\{013\}$ that are almost degenerate. The W EAM potential reproduces this trend both qualitatively and quantitatively, except for the $\Sigma3\langle110\rangle\{111\}$ GB that is largely overestimated.

Table 4 – Comparison of the GB energy calculated by DFT and EAM.

Grain boundary	DFT (mJ/m²)	EAM (mJ/m²)
$\Sigma3\langle110\rangle\{111\}$	2227	2734
$\Sigma3\langle110\rangle\{112\}$	673	640
$\Sigma5\langle100\rangle\{013\}$	2191	2092

The binding energy of a Re atom to the $\Sigma3\langle110\rangle\{111\}$ (one Re per $4\sqrt{3}a_0^2$), $\Sigma3\langle110\rangle\{112\}$ (one Re per $2\sqrt{6}a_0^2$) and $\Sigma5\langle100\rangle\{013\}$ (one Re per $2\sqrt{10}a_0^2$) are presented in Fig. 4a, b and c, respectively. The DFT data suggest attractive interactions for all GBs and at any distance from the GB plane. This is consistent with similar DFT calculations presented in [62]. For all GBs maximum attraction is observed just above the GB plane, with the least strong attraction (~0.25 eV) for the GB with lowest γ_{GB}, i.e., $\Sigma3\langle110\rangle\{112\}$ and the strongest attraction by about a factor two (~0.5 eV) for the high energy GBs.

With respect to EAM some deviations are observed. For both $\Sigma3\langle110\rangle\{111\}$ and $\Sigma5\langle100\rangle\{013\}$ attraction is only reproduced for the Re atom just above the GB plane. For all other positions the interaction is repulsive. At the point of maximum attraction EAM underestimates the attraction by about a factor two. For the low energy $\Sigma3\langle110\rangle\{112\}$ GB, on the other hand, attraction at any distance from the GB plane is reproduced by EAM.

The underestimation of the binding energy is consistent with the underestimation of the Re-v binding, which provides a measure of the binding between Re and open volume defects, such as a GB. Besides the Re-v binding energy, none of the GB configurations were included in the fit of the EAM potential.

(a)   (b)   (c)
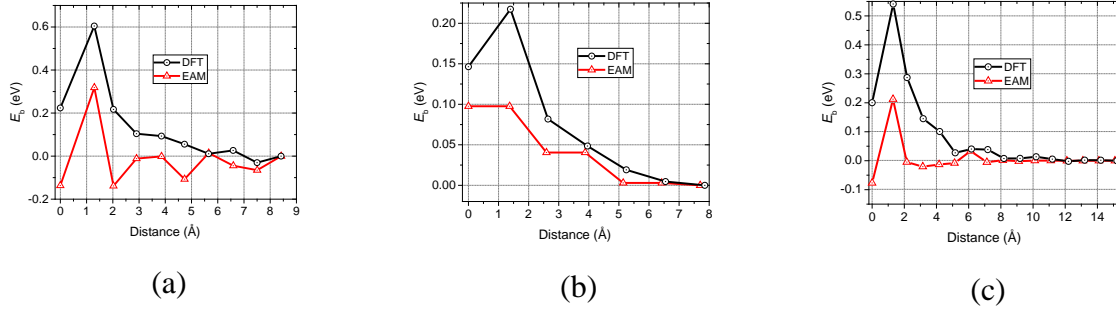
Fig. 4 – Comparison between DFT and EAM of the binding energy as a function of distance to the GB for the (a) Σ3⟨110⟩{111}; (b) Σ3⟨110⟩{112} and (c) Σ5⟨100⟩{013} GBs.

3.5. Elastic Constants

To guarantee a physical shape of both the Re-Re and W-Re pair potentials, the EAM potential was fitted with low priority to Rose's equation of state [29]. For the Re-Re pair potential the reference was hcp Re while for the W-Re pair potential the reference was the σ-phase compound with lowest formation energy as reported in [30].

In Fig. 5 the average lattice energy, $E^* = E/E_c$, under uniform expansion and contraction (with strain $a^* = 9\Omega B/E_c(a/a_0 - 1)$ and B the bulk modulus) calculated by EAM for the different reference states is compared with Rose's universal equation of state [29]. Clearly, the curves for both hcp Re and the σ W2Re are in excellent agreement with Rose's equation of state.
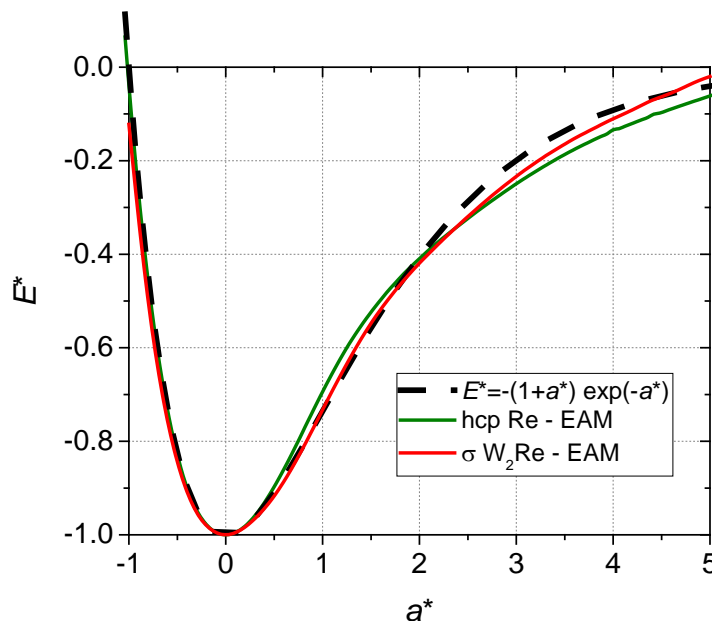
– Comparison of the equation of state for hcp Re and the σ-phase obtained by EAM with Rose's universal equation of state.

In the following, the elastic constants at both zero K and finite temperature were estimated as the average over 100 independently generated randomly disordered solid solutions in the boxes described in Table 1. The resulting statistical error is ~1GPa.

In Fig. 6 a comparison between experiment [12] and EAM is provided for different shear moduli of several bcc W-Re solid solutions at zero Kelvin. In the figure we considered the limiting cases for the shear modulus: C_{44} as upper boundary and $C' = (C_{11} - C_{12})/2$ as lower boundary. In addition, we added the shear modulus corresponding to <111> {110} shear deformation, which is the shear modulus encountered by dislocation glide in the {110} slip system.

The experimental data show that C_{44} goes through a minimum at 3% Re before increasing again. The other shear moduli, on the other hand, exhibit monotonous decrease with Re content. These data are consistent with the experimental observation of softening of W-Re alloys (0-10% Re) (see [13] and references therein). In addition, the reduction of C' indicates a reduction of the mechanical stability of the bcc phase, which is consistent with the appearance of the intermetallic σ- and χ-phases in the phase diagram for larger Re content [63]. Clearly, EAM reproduces these features.
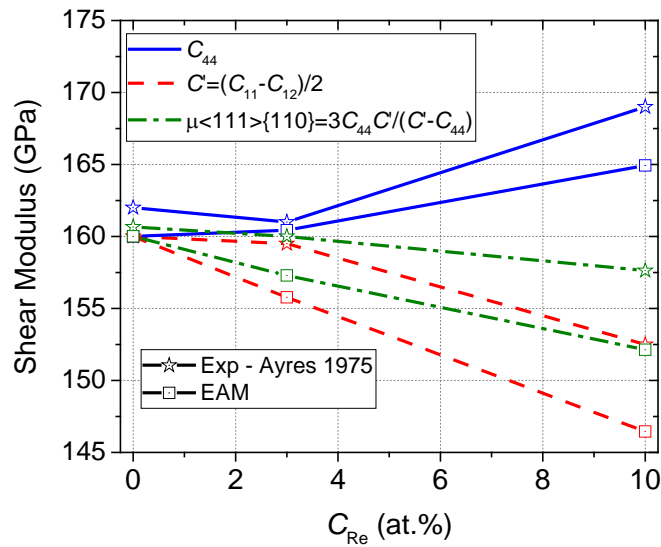
Fig. 6 – Comparison between experiment [12] and EAM for different shear moduli for several bcc W-Re solid solutions.

In Fig. 7 a and b the Voigt average of the bulk- (B_V) and shear modulus (G_V) at zero K calculated by EAM is presented as a function of composition for the various stable phases following the phase diagram. Where available, experimental data (bcc phase) [12] and DFT data (σ-phase) [30] were added for reference. Given the complex structure of both σ- and χ-phases, we discuss B_V and G_V rather than the individual elastic constants. The latter values provide a measure for the resistance against uniform deformation and shear deformation of a polycrystal. In an effort not to overload the figure, we emphasized B_V and G_V in their stability range as predicted by the phase diagram. However, the extrapolations outside the stability range can still be followed in the same figure. Detailed tables containing all independent elastic constants, mixing enthalpy and equilibrium lattice constants corresponding to the different phases are provided in Appendix B.

Both σ- and χ-phases are so called topologically closed packed (tcp) phases [64], which have a well-defined crystallographic structure but no fixed stoichiometry. As a result, they exist in a large homogeneity range, although complete disorder is never observed as their non-equivalent sites exhibit preferential occupancy. The σ-phase is a tetragonal phase described by the *P4₂/mmm* (No. 136) space group with five non-equivalent positions while the χ-phase is a cubic phase described by the $I\bar{4}3m$ (No. 217) space group with four non-equivalent positions. In the work by Crivello et al [65] the partial occupancies of the non-equivalent positions are calculated as a function of global Re content, based on simple thermodynamic considerations. The simulation boxes were prepared consistent with the data reported at 1873 K, which is in close agreement with experimental observations. As mentioned above, the estimated elastic constants are the result of an average over 100 independent random solid solutions. For all phases the statistical error was ~1 GPa.

Within the limits of the thermodynamic stability of each phase, B_V increases quasi linearly from 310 GPa for bcc W up to 382 GPa for hcp Re, thereby passing through the σ-phase (~330 GPa at 50% Re) and χ-phase (350 GPa at 80% Re). Both the experimental data for the bcc phase (0-10% Re) and DFT data for the σ-phase (30-70% Re) are well reproduced by EAM. Outside the thermodynamic stability range of the σ-phase, however, EAM fails to reproduce the linear trend predicted by DFT. This incorrect trend is due to the large overestimation of B_V for pure σ-phase W.

For the bcc phase G_V remains quasi constant in the range 0-10% Re, but sharply increases outside this Re range. For hcp Re G_V is similar to that of bcc W, but it reduces fast

with the addition of W. In depth analysis shows that the hcp phase becomes mechanically unstable below 70% Re. In their respective thermodynamic stability range, G_V for the σ-phase is higher than for the χ-phase, but both are lower than G_V for the bcc and hcp phases. Within the thermodynamic stability range the experimental G_V for the bcc phase (0-10% Re) is well reproduced. For the σ-phase agreement with the DFT data is reasonable (30-70% Re). Similar as for B_V, outside the thermodynamic stability range for the σ-phase the DFT trend for G_V is not well reproduced, which is in part due to the large overestimation of G_V for pure σ-phase W.

Thus, the experimentally observed hardening and embrittlement due to σ- and χ-phase precipitation [13, 66, 67] is unlikely to originate from the matrix precipitate shear modulus misfit. It is rather linked to the non-coherent structure of the matrix-precipitate interface, which implies impenetrable behavior of the σ- or χ-phase precipitate and overall resulting in the strong pinning of the dislocations that must overcome such inclusions by either Orowan or cross-slip mechanisms. Earlier, this phenomenon was studied and proven (both experimentally and theoretically) for Fe-Cu alloys [68]. The present EAM potential will help elucidate this in our further works.
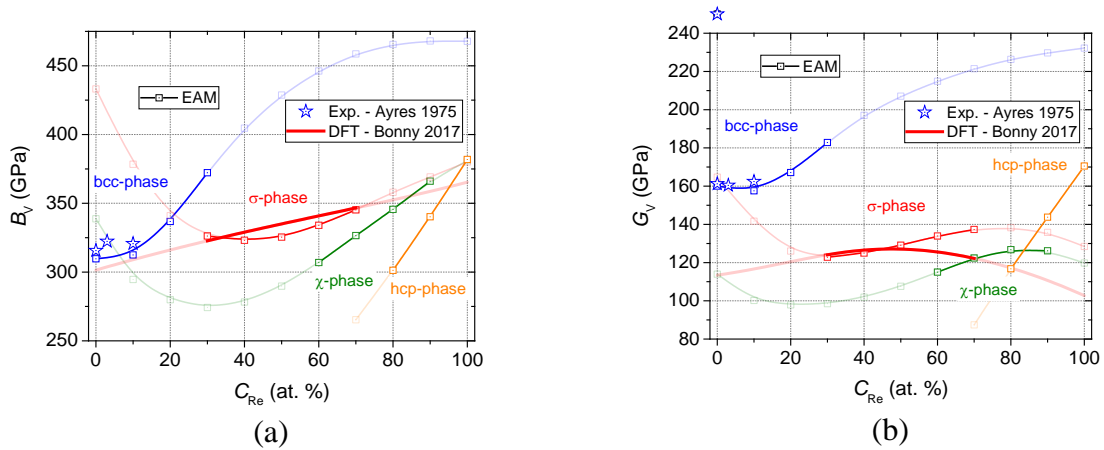
Fig. 7 – Comparison of the Voigt average of the (a) bulk modulus and (b) shear modulus between EAM, available experimental [12] and DFT [30] data for the different phases.

The evolution of the mixing enthalpy, H_{mix}, or formation energy per atom, at zero K of the bcc, σ, χ, and hcp phases with composition is summarized in Fig. 8 together with available DFT data [30, 65]. For all phases bcc W and hcp Re were used as reference states. For EAM the same configurations and statistics were used to compute the elastic constants

(see Fig. 7) while for DFT compounds corresponding to all permutations of W and Re on the non-equivalent sublattices were used (see [30, 65]). Even though H_{mix} predicted by EAM lays within the DFT range (0-0.35 eV/at.), at any composition the bcc or hcp phase is energetically more favorable. This means that at least at low temperature, both σ- and χ-phases are thermodynamically unfavorable, which is consistent with both experimental and calculated phase diagrams [65].
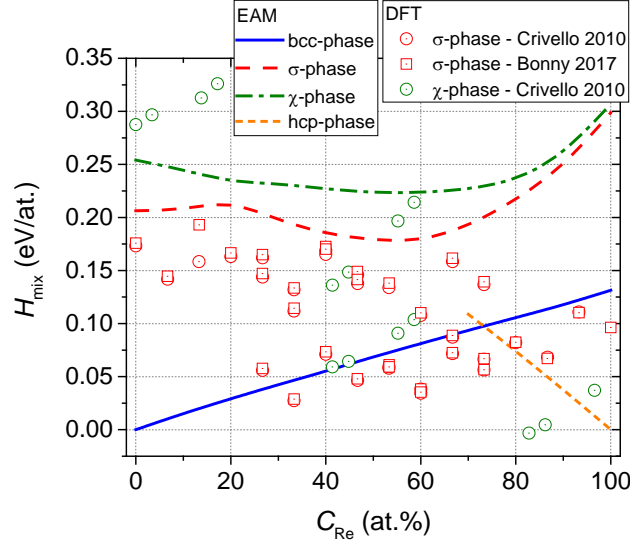

Fig. 8 – Evolution of the mixing enthalpy with composition for the bcc, σ, χ, and hcp phases with composition. DFT data [30, 65] for ordered compounds is superposed.

To ensure the stability of all phases during MD simulations at finite temperature, we studied the mechanical stability of bcc W, σ W-50%Re, χ W-75%Re and hcp Re in the temperature range 300-1500 K. For this, the same configurations and statistics were used as in Fig. 7, resulting in a statistical error of a few GPa. The necessary and sufficient conditions for mechanical stability of a given phase is a positive definite stiffness matrix for that phase, which is equivalent with strictly positive eigenvalues of the latter. For a cubic crystal (e.g. bcc and χ-phase) this leads to the following conditions [69],

$$\begin{cases} C_{11} - C_{12} > 0 \\ C_{11} + 2C_{12} > 0 \\ \quad C_{44} > 0 \end{cases}, \tag{4}$$

For a tetragonal (I) phase (e.g. hcp and the σ-phase), the necessary and sufficient conditions are given as [69],

$$\begin{cases} C_{11} - |C_{12}| > 0 \\ C_{33}(C_{11} + C_{12}) - 2C_{13}^2 > 0 \\ C_{44} > 0 \\ C_{66} > 0 \end{cases}, \tag{5}$$

where for hcp crystals the following relation $C_{66} = (C_{11} - C_{12})/2$ is valid.

In Fig. 9 the evolution with temperature of the lowest shear moduli (see criteria 4 and 5) for bcc W, σ W-50%Re, χ W-75%Re and hcp Re is summarized. These shear moduli are the most critical to satisfy criteria 4 and 5. Clearly, all shear moduli are well above zero leading to the conclusion that the investigated phases are mechanically stable in the temperature range 300-1500 K. Therefore, the EAM potential is suitable for MD studies of these phases up to at least 1500 K. Detailed tables containing all independent elastic constants and equilibrium lattice constants corresponding to the different phases EAM are provided in Appendix B.

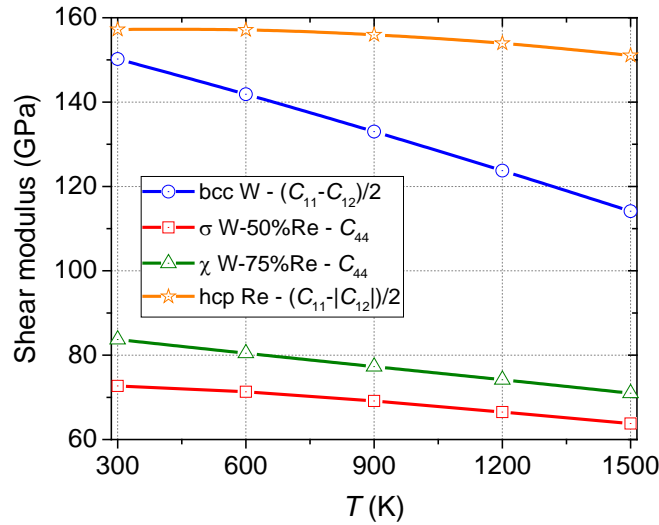

Fig. 9 – Evolution of the lowest shear moduli with temperature for bcc W, σ W-50%Re, χ W-75%Re and hcp Re.

4. Conclusive remarks

We fitted and benchmarked an EAM potential for the W-Re system against experimental and DFT data, of which a part was generated in this work.

The EAM potential was fitted to the Re formation energy in bcc W such as to reproduce large Re solubility at 700 K and above. EAM predicts the <111> W-Re dumbbell as most stable interstitial configuration with a binding energy consistent with the result of DFT calculations.

With respect to grain boundaries (GBs), EAM predicts the binding of isolated Re with a GB when placed just above the GB plane, in qualitative agreement with DFT data.

EAM reproduces the DFT predicted transition of a symmetric ½<111> screw dislocation core to an asymmetric core by alloying bcc W with Re. Also, both EAM and DFT, show a negligible effect of isolated Re on the ½<111> inter row potential and the ½<111>{110} stacking fault energy profile. The latter properties give a measure of the impact of isolated Re on the movement of a ½<111> screw and ½<111>{110} edge dislocation, respectively. Thus, the latter in combination with an asymmetric ½<111> screw dislocation core, which allows the activation of the additional {112} slip system, allows EAM to reproduce the mechanisms responsible for the experimentally observed softening of W-Re alloys.

The Voigt average of the bulk- and shear modulus for all thermodynamically stable phases, i.e., bcc, σ, χ and hcp phases were calculated. The latter provide a measure for the resistance against uniform deformation and shear deformation of a polycrystal. While B_V varies quasi linearly with Re composition for the different phases, G_V for both bcc and hcp phases are significantly higher than G_V for the σ-phase, which is in turn higher than G_V for the χ-phase.

Following the above, the hardening and embrittlement due to σ- and χ-phase precipitation should not be attributed to the shear modulus misfit strengthening mechanism. It should rather be linked to the non-coherence of the precipitates-matrix interface, a hypothesis that will be further investigated in our forthcoming works.

As a final check, the mechanical stability of bcc W, σ W-50%Re, χ W-75%Re and hcp Re was verified in the 300-1500 K temperature range. Therefore, the developed EAM potential is suitable to model W-Re alloys in bcc solid solution as well as non-coherent precipitates embedded in a bcc W matrix, at least up to a temperature of 1500 K.

In conclusion, the developed EAM potential can reproduce the mechanisms responsible for the experimentally observed softening in W-Re solid solutions and provide elastic constants in reasonable agreement with DFT data for the phases forming non-coherent

precipitates in W-Re alloys. All of this makes the presented EAM potentials an excellent tool to study plasticity in W-Re alloys at the atomic level.

Acknowledgements

Appendix A: Parameterization interatomic potential

The atomic interactions are described using the embedded atom method (EAM) [22]. In addition to pair interactions, *V*, this approach includes an embedding energy, *F*, dependent on the local electron density, ρ. The latter term approximates the many-body contribution of all nearby atoms. The total energy within EAM is given as,

$$E = \frac{1}{2}\sum_{\substack{i,j=1 \\ j \neq i}}^{N} V_{t_i t_j}(r_{ij}) + \sum_{i=1}^{N} F_{t_i}(\rho_i). \tag{A1}$$

Here *N* represents the total number of atoms in the system, r_{ij} is the distance between atoms *i* and *j*, and t_i denotes the chemical species (W or Re). The local electron density around atom *i*, contributed from its neighbors is given as,

$$\rho_i = \sum_{\substack{j=1 \\ j \neq i}}^{N} \varphi_{t_j}(r_{ij}), \tag{A2}$$

where φ denotes the electron density function of the considered element.

In this work the pair potential *V* consists of three parts: (i) equilibrium part dominated by electronic bonding, (ii) short-range part dominated by electronic repulsion and (iii) an intermediate part smoothly connecting (up to second derivative) the latter two. As such the pair potential *V* is parameterized as,

$$V_{XY}(r) = \Theta(r - r_o)\, V_{\text{eq}}(r)$$

$$+ \Theta(r_o - r)\Theta(r - r_i) \left\{ V_{\text{eq}}(r) + \zeta\left(\frac{r_o + r_i - 2r}{r_o - r_i}\right) \left[V_{\text{nucl}}(r) - V_{\text{eq}}(r) \right] \right\}$$

$$+ \Theta(r_i - r)\, V_{\text{nucl}}(r) , \tag{A3}$$

with r_i and r_o the inner and outer cut-off, respectively and Θ the Heaviside function. The short range part, V_{nucl}, is parameterized as [70],

$$V_{\text{nucl}}(r) = \frac{Q_X Q_Y}{r}\, \xi(r/r_s) , \tag{A4}$$

with Q_X and Q_Y the nuclear charges (Q_W=74 and Q_{Re}=75) and r_s=0.4683766/($Q_X^{2/3}+Q_Y^{2/3}$);

$\xi(x) = 0.1818\exp(-3.2x) + 0.5099\exp(-0.9423x) + 0.2802\exp(-0.4029) + 0.02817\exp(-0.2016),$ (A5)

and

$$\zeta(x) = \frac{3}{16}x^5 - \frac{5}{8}x^3 + \frac{15}{16}x + \frac{1}{2} . \tag{A6}$$

For both W-Re and W-W the equilibrium part is parameterized as a piecewise cubic spline,

$$V_{\text{eq}}(r) = \sum_{k=1}^{N_p}[a_k\,(r_k - r)^3\,\Theta(r_k - r)], \tag{A7}$$

with a_k the fitting coefficients and r_k the node points.

For pure W the equilibrium part follows from the effective gauge transformation [71] of parameterization "EAM2" from [24]. The effective gauge is characterized by an equilibrium density $\rho_0 = 1$ and $F^{\text{eff}\prime}(1) = 0$. The gauge transformation is given as,

$$\begin{cases} V^{\text{eff}}(r) = V(r) - 2C\,\varphi(r) \\ \quad \varphi^{\text{eff}}(r) = S\,\varphi(r) \\ F^{\text{eff}}(\rho) = F\left(\frac{\rho}{S}\right) + \frac{C}{S}\rho \end{cases} , \tag{A8}$$

with C=1.848055990 and S=2.232322602×10^{-1}.

For pure W also the embedding and density function were taken from "EAM2" in [24] and transformed following equation A8. However, the reported parameterization shows a change in curvature (from positive to negative) at about 1.35 times the equilibrium density. This change in curvature is unphysical and can lead to structural instabilities when alloyed with Re. Therefore, we modified F^{eff} beyond the inflection point to provide a positive curvature for all densities. The modified embedding function is given as,

$$F^{\text{mod}}(\rho) = \begin{cases} F^{\text{eff}}(\rho), & \rho \leq \rho_i \\ A_0 + A_1\,\rho + A_2\,\rho^2 + A_3\,\rho^3, & \rho > \rho_i \end{cases}, \qquad \text{(A9)}$$

with ρ_i =1.359141225 the inflexion point and $\{A_i\}$ spline coefficients (see Table A1) fitted to be continuous at ρ_i up to second derivative with F^{eff}. This modification does not change the equilibrium properties of the potential, such as, elastic constants, lattice stabilities, formation energy of point defects and dislocation core structure.

For pure Re the embedding function is parameterized as,

$$F(\rho) = A\,\sqrt{\rho} + B\,\rho + C\,\rho^2, \qquad \text{(A10)}$$

while the density function is parameterized as,

$$\varphi(r) = C_0(r_c - r)^3\,\Theta(r_c - r), \qquad \text{(A11)}$$

with r_c the cut-off. All fitting parameters are provided in Table A1 and a visualization of the potential functions is given in Fig. A1. These figures illustrate the smoothness of the potential functions.

Table A1 – Parameterization of the EAM potential.

Pure W	Pure Re
A_0 = -5.524855802 eV	A=-7.046791948 eV
A_1 = 2.317313103×10^{-1} eV	B=1.236584720 eV
A_2 = -3.665345949×10^{-2} eV	C=1.143405627 eV

$A_3 = 8.989367404 \times 10^{-3}$ eV

$C_0 = 3.704045964 \times 10^{-3}$ Å^{-3}

$r_c = 5.460000000$ Å

$r_i = 1.000000000$ Å $\qquad$ $r_i = 1.000000000$ Å

$r_o = 2.000000000$ Å $\qquad$ $r_o = 2.000000000$ Å

$\underline{r_k}$ (Å)	$\underline{a_k}$ (eV/Å^3)
$r_1 = 2.700000000$	$a_1 = 6.726805309$
$r_2 = 3.252000000$	$a_2 = 3.217593889$
$r_3 = 3.804000000$	$a_3 = -6.545857587 \times 10^{-1}$
$r_4 = 4.356000000$	$a_4 = 1.453229484 \times 10^{-1}$
$r_5 = 4.908000000$	$a_5 = -2.063629464 \times 10^{-1}$
$r_6 = 5.460000000$	$a_6 = 6.114909116 \times 10^{-2}$

W-Re

$r_i = 1.000000000$ Å

$r_o = 2.000000000$ Å

$\underline{r_k}$ (Å)	$\underline{a_k}$ (eV/Å^3)
$r_1 = 2.650000000$	$a_1 = -2.335000000 \times 10^{1}$
$r_2 = 2.700000000$	$a_2 = 2.456959229 \times 10^{1}$
$r_3 = 3.075000000$	$a_3 = -2.585878138$
$r_4 = 3.450000000$	$a_4 = 3.457586051$
$r_5 = 3.825000000$	$a_5 = -7.013105493 \times 10^{-1}$
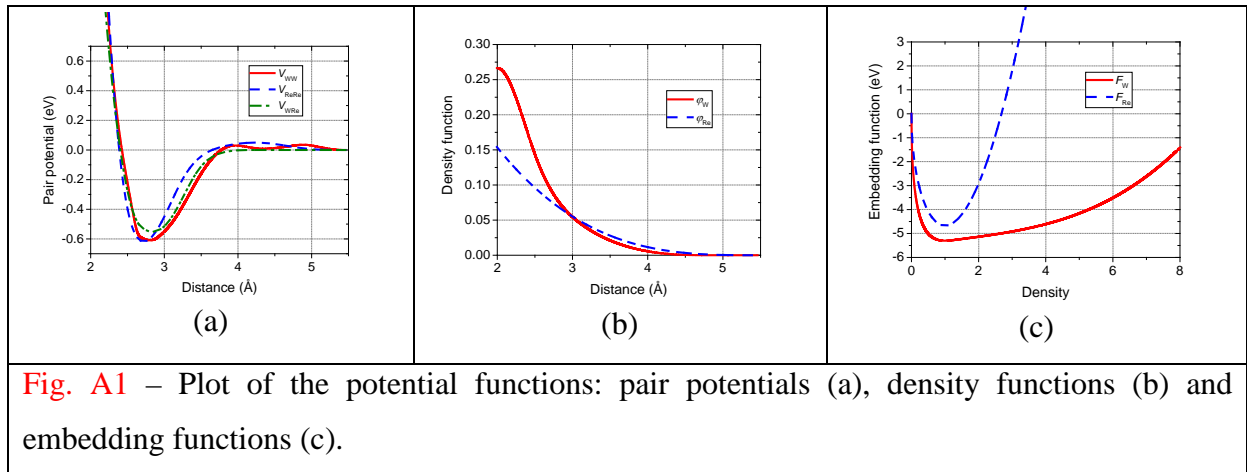
Fig. A1 – Plot of the potential functions: pair potentials (a), density functions (b) and embedding functions (c).

Appendix B: Details of the different phases

The data corresponding to the evolution of the independent elastic constants, mixing enthalpy and lattice parameters with composition for the bcc, σ, χ and hcp phases on which Figs. 7 and 8 are based are presented in Tabs B1, B2, B3 and B4, respectively.

The data corresponding to the evolution of the independent elastic constants, critical shear moduli (see equations 4 and 5) and elastic constants with temperature for bcc W, σ W-50%Re, χ W-75%Re and hcp Re on which Fig. 9 is based are presented in Tabs B5, B6, B7 and B8, respectively.

In Fig. A1 a comparison between experiment [42, 72] and EAM of the evolution of the lattice constants with temperature for bcc W and hcp Re is given. For bcc W EAM underestimates the experimental lattice parameter [42]. The thermal expansion coefficients in the plotted temperature range, on the other hand, are similar with 5.2×10^{-6} and 6.3×10^{-6} for the experimental and EAM data, respectively.

For hcp W, EAM reproduces both a and c parameters in the experimental range. With respect to the thermal expansion in the plotted temperature range, however, only the one for a is well reproduced while EAM underestimates the experimental one by almost a factor three (see also Table 2).
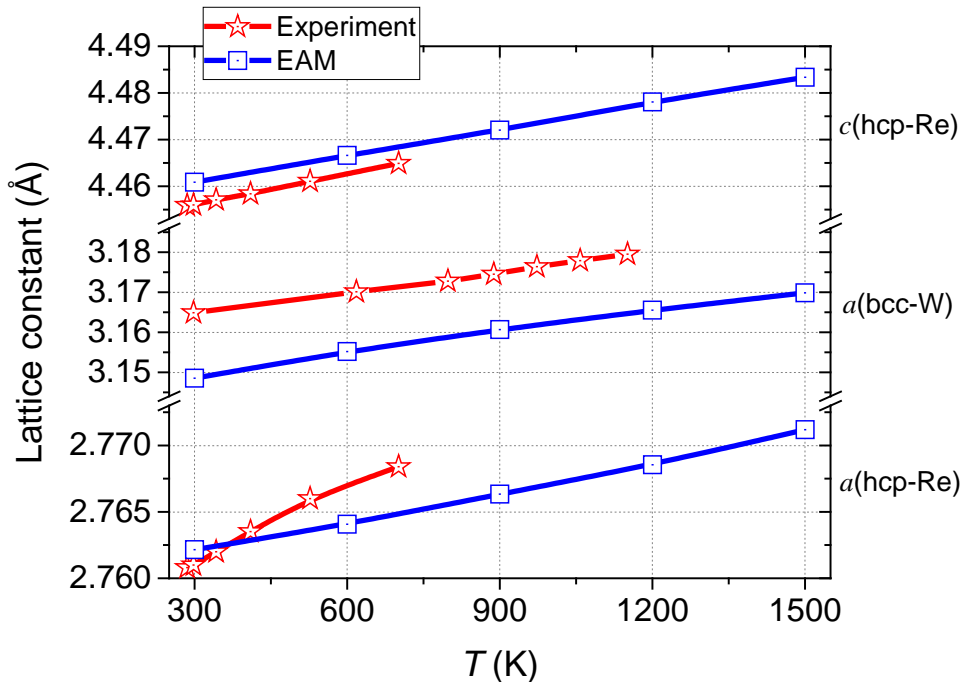

Fig. B1 – Comparison between experiment [42, 72] and EAM of the evolution of the lattice constants with temperature for bcc W and hcp Re.

Table B1 – Evolution of the independent elastic constants, mixing enthalpy and lattice parameters with composition for the bcc phase.

C_{Re} (at.%)	C_{11} (GPa)	C_{12} (GPa)	C_{44} (GPa)	H_{mix} (eV/at.)	a (Å)
0	523	203	160	0.000	3.140
10	508	215	165	0.015	3.129
20	515	248	189	0.029	3.119
30	535	291	223	0.042	3.109
40	552	331	254	0.055	3.100
50	562	362	278	0.069	3.091
60	567	386	298	0.081	3.082
70	567	404	315	0.094	3.073
80	562	417	329	0.106	3.064
90	554	425	340	0.117	3.056
100	541	431	350	0.131	3.048

Table B2 – Evolution of the independent elastic constants, mixing enthalpy and lattice parameters with composition for the σ-phase.

C_{Re} (at.%)	C_{11} (GPa)	C_{33} (GPa)	C_{12} (GPa)	C_{13} (GPa)	C_{44} (GPa)	C_{66} (GPa)	H_{mix} (eV/at.)	a (Å)	c (Å)
0	1034	295	513	127	63	166	0.206	9.538	5.070
10	863	312	438	123	57	142	0.207	9.531	5.074
20	735	346	379	124	55	125	0.216	9.524	5.079
30	678	380	340	130	58	120	0.197	9.519	5.074
40	647	429	312	140	63	121	0.185	9.512	5.062
50	633	475	290	152	69	124	0.178	9.503	5.043
60	636	524	281	162	73	127	0.178	9.490	5.023
70	644	580	279	170	72	126	0.192	9.473	5.005
80	654	644	284	175	65	122	0.216	9.450	4.989
90	661	709	292	177	52	113	0.248	9.426	4.976
100	667	779	307	173	26	104	0.299	9.395	4.963

Table B3 – Evolution of the independent elastic constants, mixing enthalpy and lattice parameters with composition for the χ-phase.

C_{Re} (at.%)	C_{11} (GPa)	C_{12} (GPa)	C_{44} (GPa)	H_{mix} (eV/at.)	a (Å)
0	530	243	94	0.254	9.711

10	456	214	87	0.245	9.696
20	437	201	85	0.233	9.683
30	434	194	84	0.232	9.670
40	448	193	85	0.227	9.656
50	476	196	86	0.223	9.639
60	515	203	88	0.223	9.616
70	556	211	89	0.227	9.586
80	594	221	87	0.235	9.553
90	631	233	78	0.259	9.515
100	661	241	60	0.307	9.476

Table B4 – Evolution of the independent elastic constants, mixing enthalpy and lattice parameters with composition for the hcp phase.

C_{Re} (at.%)	C_{11} (GPa)	C_{33} (GPa)	C_{12} (GPa)	C_{13} (GPa)	C_{44} (GPa)	H_{mix} (eV/at.)	a (Å)	c (Å)
70	363	500	255	162	85	0.109	2.777	4.519
80	455	541	261	184	107	0.074	2.773	4.496
90	536	601	278	208	132	0.038	2.768	4.475
100	611	682	299	234	159	0.000	2.761	4.456

Table B5 – Evolution of the independent elastic constants, critical shear moduli and elastic constants with temperature for bcc W.

	300 K	600 K	900 K	1200 K	1500 K
C_{11} (GPa)	596	606	597	577	551
C_{12} (GPa)	295	323	331	330	323
C_{44} (GPa)	253	281	291	291	286
$\frac{C_{11}-C_{12}}{2}$ (GPa)	150	142	133	124	114
$\frac{C_{11}+2C_{12}}{3}$ (GPa)	395	417	420	412	399
a (Å)	3.149	3.155	3.161	3.166	3.170

Table B6 – Evolution of the independent elastic constants, critical shear moduli and elastic constants with temperature for σ W-50%Re.

	300 K	600 K	900 K	1200 K	1500 K
C_{11} (GPa)	579	554	531	508	486
C_{33} (GPa)	527	536	533	524	511

C_{12} (GPa)	249	236	225	216	208
C_{13} (GPa)	163	161	158	154	151
C_{44} (GPa)	73	71	69	67	64
C_{66} (GPa)	124	120	114	109	104
$\frac{C_{11}-|C_{12}|}{2}$ (GPa)	165	159	153	146	139
$\frac{C_{33}(C_{11}+C_{12})-2C_{13}^2}{4}$ (GPa^2)	95936	92815	88267	82910	77298
a (Å)	9.520	9.538	9.556	9.573	9.591
c (Å)	5.041	5.044	5.048	5.054	5.060

Table B7 – Evolution of the independent elastic constants, critical shear moduli and elastic constants with temperature for χ W-75%Re.

	300 K	600 K	900 K	1200 K	1500 K
C_{11} (GPa)	562	551	541	527	513
C_{12} (GPa)	212	208	203	198	192
C_{44} (GPa)	84	80	77	74	71
$\frac{C_{11}-C_{12}}{2}$ (GPa)	175	172	169	165	160
$\frac{C_{11}+2C_{12}}{3}$ (GPa)	329	322	316	308	299
a (Å)	9.582	9.594	9.605	9.618	9.631

Table B8 – Evolution of the independent elastic constants, critical shear moduli and elastic constants with temperature for hcp Re.

	300 K	600 K	900 K	1200 K	1500 K
C_{11} (GPa)	616	617	616	611	602
C_{33} (GPa)	692	695	694	689	679
C_{12} (GPa)	302	303	304	302	299
C_{13} (GPa)	236	236	236	233	230
C_{44} (GPa)	160	160	159	157	154
$\frac{C_{11}-|C_{12}|}{2}$ (GPa)	157	157	156	154	152
$\frac{C_{33}(C_{11}+C_{12})-2C_{13}^2}{4}$ (GPa^2)	130830	131898	131663	129907	126562
a (Å)	2.763	2.765	2.763	2.768	2.771
c (Å)	4.458	4.460	4.475	4.478	4.484

References

[1] Zinkle S J and Busby J T 2009 *Mater. Today* **12** 12

[2] Zinkle S J 2005 *Phys. Plasmas* **12** 058101

[3] Matsuda S and Tobita K 2013 *J. Nucl. Sci. Technol.* **50** 321

[4] Rieth M, Armstrong D, Dafferner B, Heger S, Hoffmann A, Hofmann M-D and Jäntsch U 2010 *Adv. Sci. Technol.* **73** 11

[5] Giannattasio A, Yao Z, Tarleton E and Roberts S G 2010 *Philos. Mag.* **90** 3947

[6] Hasegawa A, Fukuda M, Nogami S, Yabuuchi K 2014 *Fusion Eng. Des.* **89** 1568

[7] Gorynin I V, Ignatov V A, Rybin V V, Fabritsiev S A, Kazakov V A, Chakin V P, Tsykanov V A, Barabash V R and Prokofyev Y G 1992 *J. Nucl. Mater.* **191** 421

[8] Steichen J M 1976 *J. Nucl. Mater.* **60** 13

[9] Stork D, Agostini P, Boutard J L, Buckthorpe D, Diegele E, Dudarev S L, English C, Federici G, Gilbert M R, Gonzalez S, Ibarra A, Linsmeier C, Li Puma A, Marbach G, Morris P F, Packer L W, Raj B, Rieth M, Tran M Q, Ward D J and Zinkle S J 2014 *J. Nucl. Mater.* **455** 277

[10] Bolt H, Barabash V, Krauss W, Linke J, Neu R, Suzuki S, Yoshida N and Team A U 2004 J. Nucl. Mater. **329** 66

[11] Fukuda M, Yabuuchi K, Nogami S, Hasegawa A and Tanaka T 2014 *J. Nucl. Mater.* **455** 460

[12] Ayres R A, Shannette G W and Stein D F 1975 *J. Appl. Phys.* **46** 1526

[13] Bryskin B D and Carlén J-C 1996 *Mater. Manuf. Process.* **11** 67

[14] Stephens J and Witzke W 1976 *J. Less-Common Met.* **48** 285

[15] Blomerus P M, Hills D A and Kelly P A 1999 *J. Mech. Phys. Solids* **47** 1007

[16] Clayton J D 2005 *J. Mech. Phys. Solids* **53** 261

[17] Terentyev D, Xiao X Z, Dubinko A, Bakaeva A and Duan H L 2015 *J. Mech. Phys. Solids* **85** 1

[18] Xiao X Z, Terentyev D, Yu L, Song D K, Bakaev A and Duan H L 2015 *J. Nucl. Mater.* **466** 312

[19] Xiao X Z, Terentyev D, Yu L, Bakaev A, Jin Z H and Duan H L 2016 *J. Nucl. Mater.* **477** 123

[20] McVeigh C and Liu W K 2009 *J. Mech. Phys. Solids* **57** 244

[21] McVeigh C and Liu W K 2010 *J. Mech. Phys. Solids* **58** 187

[22] Daw M S and Baskes M I 1984 *Phys. Rev. B* **29** 6443

[23] Bonny G, Terentyev D, Bakaev A, Grigorev P and Van Neck D 2014 *Modelling Simul. Sci. Eng.* **22** 053001

[24] Marinica M-C et al 2013 *J. Phys. Condens. Matter* **25** 395502

[25] Bonny G, Grigorev P and Terentyev D 2014 *J. Phys. Condens. Matter.* **26** 485001

[26] Grigorev P, Terentyev D, Bonny G, Zhurkin E E, Van Oost G and Noterdaeme J-M 2015 *J. Nucl. Mater.* **465** 364

[27] Grigorev P, Terentyev D, Bonny G, Zhurkin E E, Van Oost G and Noterdaeme J-M 2016 *J. Nucl. Mater.* **474** 143

[28] Grigorev P, Terentyev D A, Bakaev A V and Zhurkin E E 2016 *J. Surf. Invest.* **10** 398

[29] Rose J H, Smith J R, Guinea F and Ferrante J 1984 *Phys. Rev. B* **29** 2963

[30] Bonny G, Bakaev A, Terentyev D and Mastrikov Yu A 2017 *Scr. Mater.* **128** 45

[31] Bonny G, Pasianot R C and Malerba L 2009 *Phil. Mag.* **89** 711

[32] Bonny G, Pasianot R C and Malerba L 2009 *Phil. Mag.* **89** 3451

[33] Kresse G and Hafner J 1993 *Phys. Rev. B* **47** 558

[34] Kresse G and Furthmuller J 1996 *Phys. Rev. B* **54** 11169

[35] Blochl P E 1994 *Phys. Rev. B* **50** 17953

[36] Kresse G and Joubert D 1999 *Phys. Rev. B* **59** 1758

[37] Perdew J P, Chevary J A, Vosko S H, Jackson K A, Pederson M R, Singh D J and Fiolhais C 1992 *Phys. Rev. B* **46** 6671

[38] Vosko S H, Wilk L and Nusair M 1980 *Can. J. Phys.* **58** 1200

[39] Monkhorst H J and Pack J D 1976 *Phys. Rev. B* **13** 5188

[40] Methfessel M and Paxton A T 1989 *Phys. Rev. B* **40** 3616

[41] Plimpton S 1995 *J Comp Phys* **117** 1

[42] Liu L-G, Takahashi T and Bassett W A 1970 *J. Phys. Chem. Solids* **31** 1345

[43] Kittel C 1996 *Introduction to Solid State Physics*, seventh edn (New York: JohnWiley & Sons)

[44] Wang Y, Cutarolo S, Jiang C, Arroyave R, Wang T, Ceder G, Chen L-Q and Liu Z-K 2004 *CALPHAD* **28** 79

[45] Shepard M L and Smith J F 1965 *J. Appl. Phys.* **36** 1447

[46] Cai W and Nix W D 2016 *Imperfections in Crystalline Solids* (Cambridge: Cambridge University Press)

[47] Jaffee R I, Sims C T and Harwood J J 1958 *The Effect of Rhenium on the Fabricability and Ductility of Molybdenum and Tungsten*, 3rd Plansee Seminar Proceedings (New York: Pergamon Press) 380

[48] Bonny G, Pasianot R C, Zhurkin E E and Hou M 2011 Comp. Mater. Sci. 50 2216

[49] Gharaee L and Erhart P 2015 *J. Nucl. Mater.* **467** 448

[50] Suzudo T, Yamaguchi M and Hasegawa A 2014 *Modelling Simul. Mater. Sci. Eng.* **22** 075006

[51] Becquart C S, Domain C, Sarkar U, DeBacker A and Hou M 2010 *J. Nucl. Mater.* **403** 75

[52] Becquart C and Domain C 2007 *Nucl. Instrum. Methods Phys. Res. B* **255** 23

[53] Romaner L, Ambrosch-Draxl C and Pippan R 2010 *Phys. Rev. Lett.* **104** 195503

[54] Vitek V, Perrin R C and Bowen D K 1970 *Phil. Mag.* **21** 1049

[55] Li H, Wurster S, Motz C, Romaner L, Ambrosch-Draxl C and Pippan R 2012 *Acta Mater.* **60** 748

[56] Samolyuk G D, Osetsky Y N and Stoller R E 2013 *J. Phys. Condens. Matter* **25** 025403

[57] Frederiksen S L and Jacobsen K W 2003 *Phil. Mag.* **83** 365

[58] Ismail-Beigi S and Arias T A 2000 *Phys. Rev. Lett.* **84** 1499

[59] Ventelon L and Willaime F 2007 *J. Comput. Aided Mater. Des.* **14** (suppl. 1) 85

[60] Kaburaki H, Shimizu F, Ogata S, Yamaguchi M, Kano T, Kimizuka H and Itakura M 2007 Annual Report on Earth Simulator Center

[61] Shimizu F, Ogata S, Kano T, Li J and Kaburaki H 2007 *J. Earth Simulator* **7** 17

[62] Wu X, You Y-W, Kong X-S, Chen J-L, Luo G-N, Lu G-H, Liu C S and Wang Z 2016 *Acta Mater.* **120** 315

[63] Massalski T B, Okamoto H, Subramanian P R and Kacprzak L 2007 *Binary Alloy Phase Diagram,* second edn (ASM International)

[64] Frank F C and Kasper J S 1958 *Acta Crystallogr.* **11** 184

[65] Crivello J-C and Joubert J-M 2010 *J. Phys. Condens. Matter* **22** 035402

[66] Peckner D and Burnstein M 1977 *Handbook of Stainless Steels* (New York: McGraw-Hill)

[67] Rae C M and Reed R C 2001 *Acta Mater.* **49** 4113

[68] Minov B, Terentyev D, Van Renterghem W, Osetsky Y and Konstantinovic M J 2014 *Mater. Sci. Eng. A* **597** 46

[69] Mouhat F and Coudert F-X 2014 *Phys. Rev. B* **90** 224104

[70] Ziegler J F, Biersack J P and Littmark U 1985 *The Stopping and Range of Ions in Matter* (New York: Pergamon)

[71] Bonny G and Pasianot R C 2010 *Phil. Mag. Lett.* **90** 559

[72] Dutta B N and Dayal B 1963 *Phys. Stat. Sol.* **3** 2253